A novel rotary-cavity reactor for sustainable solar metallurgy: Design and experimental demonstration of direct reduction of iron ore

Stéphane Abanades, Roger Garcia, Jian Cong

Chemical Engineering Journal 505 (2025) 159441

Contents lists available at ScienceDirect

Chemical Engineering Journal

journal homepage: www.elsevier.com/locate/cej

A novel rotary-cavity reactor for sustainable solar metallurgy: Design and experimental demonstration of direct reduction of iron ore

Stéphane Abanades [a,*], Roger Garcia [a], Jian Cong [a,b]

[a] CNRS, Processes, Materials and Solar Energy Laboratory (PROMES), 7 rue du Four Solaire, 66120 Odeillo Font-Romeu, France
[b] University of Chinese Academy of Sciences, Beijing 100049, China

ARTICLE INFO

Keywords:
Direct reduced iron
Solar steel metallurgy
Rotary kiln
Solar reactor
Hydrogen reduction
Iron making decarbonation
Solid particles processing

ABSTRACT

This study addresses the direct reduction of iron ore with hydrogen and solar energy as the process heat source for clean iron/steel making and decarbonation of the metallurgical process. A novel rotary-type solar reactor was designed, constructed and tested for demonstration of hydrogen-based direct iron ore reduction under real direct solar irradiation. Such a solar reactor concept for clean ironmaking has never been implemented before. The reactor was first simulated to determine the temperature field, gas velocity, and H_2 mole fraction contours in the directly-heated cavity for design validation. The on-sun experimental study focused on reactor testing and performance analysis (including Fe products yields and quality). The effect of increasing temperature (>900–1000 °C at the cavity center, depending on cavity size) or H_2 flow rate (0.5–1–2 NL/min), and decreasing particle size on promoting the reduction extent was emphasized. Two different cavity designs and materials (stainless steel and mullite) were also considered to show their impact on the process performance. Using a ceramic cavity with smaller diameter allowed reaching higher temperatures over 1000 °C at its center, with faster heating rates and enhanced conversion. High Fe_2O_3 particle conversion up to 100 % was obtained based on continuous quantification of the H_2 consumed by the reduction reaction. Solid products analysis (XRD, SEM/EDX) confirmed the production of pure Fe by the solar-driven process, therefore offering a promising route toward sustainable solar metallurgy.

1. Introduction

Decarbonation of the iron and steel making industry represents a major challenge to reduce the CO_2 emissions from this energy-intensive sector. Steel is mainly produced by reducing iron ore through the blast furnace – basic oxygen furnace route (BF-BOF) or by recycling steel scrap in an electric arc furnace (EAF). Iron and steel sector releases ~7 % of total CO_2 emission and 16 % of total industrial emission [1]. The BF-BOF route uses approximately 18 GJ/t of energy supplied from coal, and has an emission intensity of ~1.87 t_{CO2}/t_{steel}, 70 % of greenhouse gas (GHG) emissions coming from the reduction step using coke and coal [2–4]. As an alternative route, direct reduction of iron (DRI) consists in extracting oxygen from chemical reduction of iron ore (in pellet and/or lumpy form) or other iron bearing materials in solid state reactions, thus without involving its melting as in the blast furnace process. The so-produced sponge iron is then melted with carbon in EAF to produce steel. Different reducing agents can be considered such as H_2 and CO produced from reformed natural gas, syngas, or coal. However, the coal or natural gas-based DRI process still generates GHG emissions and requires carbon capture and storage (CCS) to reduce its carbon footprint. Using carbon-free or bio-based reducers (e.g., H_2, NH_3, biogas, biomass, etc.) is thus a suitable option to eliminate CO_2 emissions of the reduction step. For instance, the DRI process with H_2 is based on the following global reduction reaction [5]:

$$Fe_2O_3 + 3H_2 \rightarrow 2Fe + 3H_2O(g)\ \Delta H^\circ = 97.5\ kJ/mol \quad (1)$$

Below 570 °C, magnetite (Fe_3O_4) is the only formed intermediate before reduced iron. Above 570 °C, hematite (Fe_2O_3) is first reduced to magnetite and wuestite (FeO), and the reduction of FeO to Fe is the limiting step of the overall reaction kinetics. The reduction mechanism of iron ore with H_2 or syngas has been previously investigated [6–8] and several parameters affect the kinetics [8–11]. The use of NH_3 reducer was also considered [12]. Hydrogen reduction for steelmaking represents a CO_2-free approach, provided that green hydrogen from renewables can be produced in sufficient amounts [13]. The most common route for green H_2 is electrolysis of water, but other routes not relying on

* Corresponding author.
E-mail address: stephane.abanades@promes.cnrs.fr (S. Abanades).

https://doi.org/10.1016/j.cej.2025.159441
Received 7 October 2024; Received in revised form 31 December 2024; Accepted 8 January 2025
Available online 9 January 2025

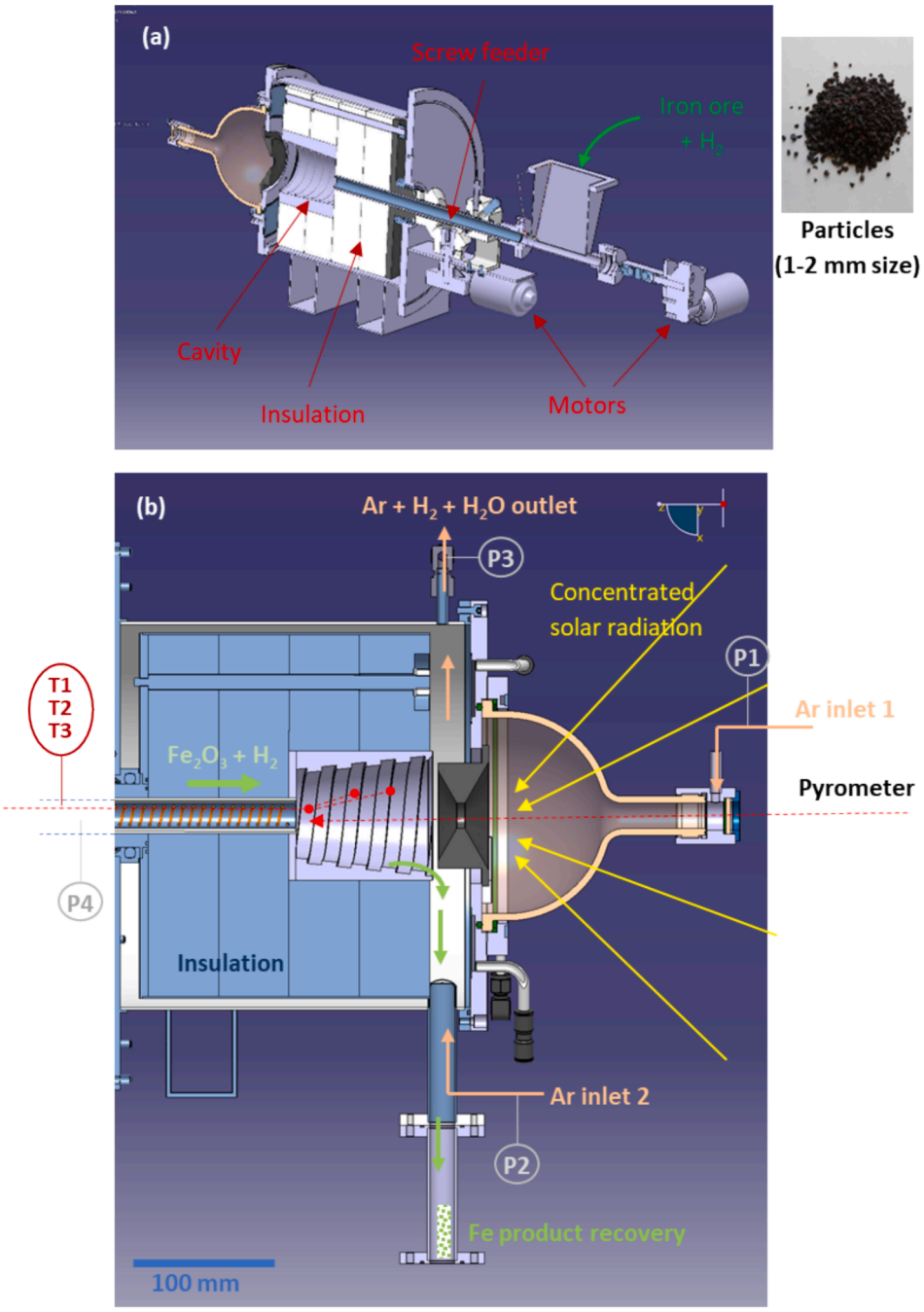

Fig. 1. Scheme of the windowed directly-irradiated cavity-type solar reactor designed for the continuous reduction of iron ore: (a) 3D cross-section, (b) 2D view of the solar reactor and operating principle with gas flow inlets/outlet and particle injection/recovery.

electricity can be considered such as solar thermochemical water-splitting [14] or pyrolysis/gasification processes [15,16].

To further reduce the carbon footprint of steel making, carbon-free energy sources should be used, such as electrical power or concentrated solar heat, to replace fossil fuels. The integration of high-temperature solar heat in industrial processes (SHIP) is a promising option for decarbonation of energy-intensive industries. High-temperature heat is delivered by concentrating solar thermal (CST) systems to solar reactors in which endothermic thermochemical reactions can be carried out. For instance, the solar thermal reduction step of Fe_3O_4 to FeO releasing O_2 was investigated as part of two-step redox cycles for H_2O and CO_2 splitting [17,18]. The use of carbonaceous reducers (CH_4, wood or waste biomass) for complete solar reduction to Fe was considered [19–22]. Besides, various solar metallurgical processes for metals production (Mg, Zn, Sn, W, Cu, etc.) involving different carbonaceous reductants such as solid carbon, biochar or methane were also investigated [23–27]. Solar H_2-based reduction of Fe_2O_3 cohesive fine powder was carried out in a vibrated fluidized bed solar reactor, reaching 98 % of reduction in 50 min [28]. Recently, the production of pure iron combined with agricultural waste biomass gasification was demonstrated in a continuously-fed solar reactor [29], and the complete reduction of iron ore with H_2 was achieved in a solar packed-bed reactor at temperatures up to 1000 °C [30].

Hydrogen has a strong potential for decarbonation of the hard-to-abate industrial and transportation sectors. Moreover, using solar energy for process heat in place of fossil fuels is a means to reduce the dependence of metallurgical processes on conventional energy resources and to avoid emissions of CO_2 and other pollutants, for the production of

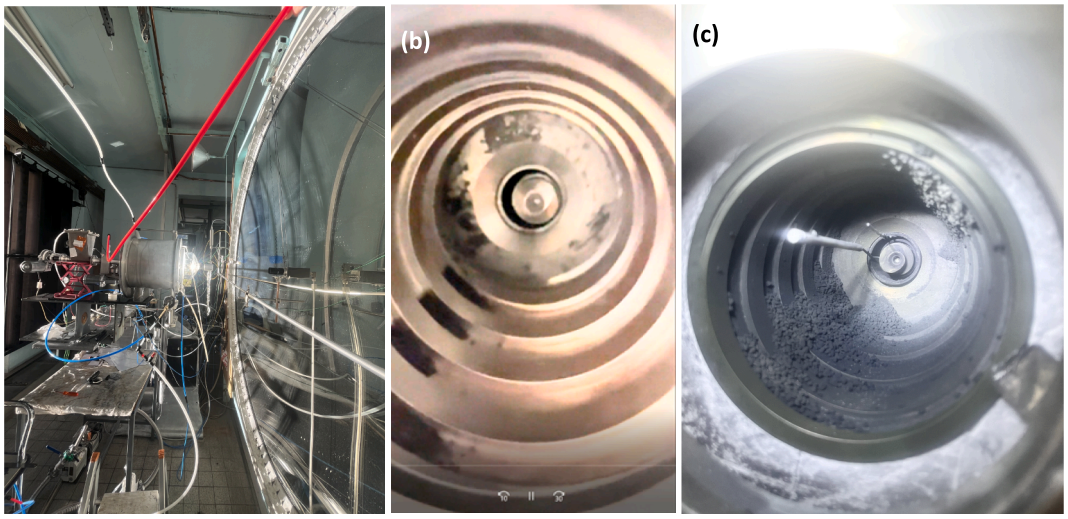

Fig. 2. Pictures of (a) solar reactor at the focus of a horizontal axis solar dish concentrator, (b) continuous particle flow with cavity rotation during cold injection tests (particles entrained to the left due to cavity rotation), (c) cold rotating cavity with three thermocouples inserted from the back and reacted iron products (the front diaphragm with small aperture closing the cavity during solar tests is not installed).

Table 1
Materials physical properties used in the CFD model.

Solid zones	Al_2O_3-SiO_2 insulation	Stainless steel [48]
Density (kg m^{-3})	400	8030
Thermal conductivity (W m^{-1} K^{-1})	$0.0196 + 0.000129 \cdot T$	$23.5 + 0.0016 \cdot (T-300)$ ($T < 1100$ K) $25.4 + 1.3 \cdot 10^{-2} \cdot (T-1100)$ ($T > 1100$ K)
Specific heat capacity (J kg^{-1} K^{-1})	$4 \cdot 10^{7} \cdot T^3 + 1.3797 \cdot 10^{3} \cdot T^2 + 1.5987289 \cdot T + 477.6995948$	$472 + 13.6 \cdot 10^{-2} \cdot T - 2.82 \cdot 10^{6} / T^2$
Fluid zones	**Argon**	**Hydrogen**
Density @298 K (kg m^{-3})	1.634	0.082
Thermal conductivity (W m^{-1} K^{-1})	$2.353 \cdot 10^{-12} \cdot T^3 - 1.289 \cdot 10^{-8} \cdot T^2 + 4.837 \cdot 10^{-5} \cdot T + 0.00483$	$-4.9 \cdot 10^{-7} \cdot T^2 + 7.856 \cdot 10^{-4} \cdot T - 5.25 \cdot 10^{-3}$
Specific heat capacity (J kg^{-1} K^{-1})	$520.32 + 7.074 \cdot 10^{-6} \cdot T - 3.664 \cdot 10^{-6} \cdot T^2$	$13359 + 2.0184 \cdot T - 1.2506 \cdot 10^{-4} \cdot T^2$

solid metallic iron. As such, the replacement of carbon-based feedstocks (such as coke and coal) combined with the use of concentrated solar heat offers a sustainable alternative pathway for clean ironmaking.

In the field of solar thermochemical processes, different solar reactor technologies have been developed for the processing of reactive particles through solid–gas reactions involved for instance in redox cycles for solar fuels synthesis, thermochemical energy storage (TCES), or cement production [31–36]. Particle reactors are usually based on packed or fluidized beds [30,37,38], rotary kilns [39–41], or entrained flow reactors (cyclone, drop tube, vortex flow, particle cloud/aerosol, etc.) [42–44]. Among these technologies, rotary reactors are particularly attractive as they offer favorable heat and mass transfer due to particle motion, versatility, and scalability since they are already widely employed in many industrial processes involving particles. Different types of solar-heated rotary kilns were developed at lab-scale for particles calcination (typically limestone calcination [39,45]) or thermal reduction of oxides (for TCES [35] or ZnO to Zn reduction [41,46]). However, such a solar reactor concept has never been implemented for direct reduction of iron ore. In addition, continuously-fed reactors for solar particles processing have scarcely been demonstrated.

In this study, a novel continuous-flow solar reactor based on rotary cavity was designed and developed, enabling direct iron ore particles feeding in the heated chamber and reaction products extraction. The production of renewable iron was never demonstrated before in a particle-fed solar reactor prototype under real concentrated solar flux. The reactor was modelled, constructed, and tested at the focus of a high-flux solar concentrator, targeting continuous iron production. The experimental performance evaluation included determination of chemical conversion of iron ore, reaction progress monitoring through continuous gas analysis, and solid products characterization. The experiments aimed to demonstrate the process feasibility of iron ore direct reduction and the reactor reliability under real concentrated solar flux, with relevant scalability potential, thus paving the way toward sustainable iron and steel production.

2. Experimental methods

2.1. Solar reactor design

The whole experimental system is composed of a solar concentrating system, a solar reactor, a particle feeding system (for iron ore injection), a solid recovery unit, and a gas analysis system for measuring outlet H_2 concentration. The novel solar reactor is based on a rotating cavity concept enabling the continuous injection and extraction of particles under controlled atmosphere (Fig. 1a). This design was developed for experimental testing of direct iron ore reduction at the focus of a horizontal axis solar furnace, and to determine the product yields as a function of the main operating parameters such as temperature, oxide particle size, or gas flow rates.

The cavity is made of stainless steel (304L) with an internal helical path (thread step: 21.11 mm, depth: 2.98 mm fixed empirically) to guide the particles during their progression on the wall along the cavity length from their injection at the back to the front of the reactor. In addition, the internal wall of the cavity is slightly inclined (5.89° angle) to favor the flow of particles toward the front, thus exhibiting a conical like shape (cavity inner diameters: 60 mm back and 80 mm front, outer diameter: 92 mm, length: 97 mm, volume: 376 cm^3). The cavity back is closed by a 5 mm thick stainless-steel plate with a central opening for the passage of the screw feeder. The cavity front is covered by a diaphragm made of alumino-silicate insulation with an 18 mm diameter aperture to let enter the concentrated solar radiation (with a 120° opening angle). This aperture allows for maximum radiation absorption inside the cavity receiver, while minimizing re-radiation losses toward the environment.

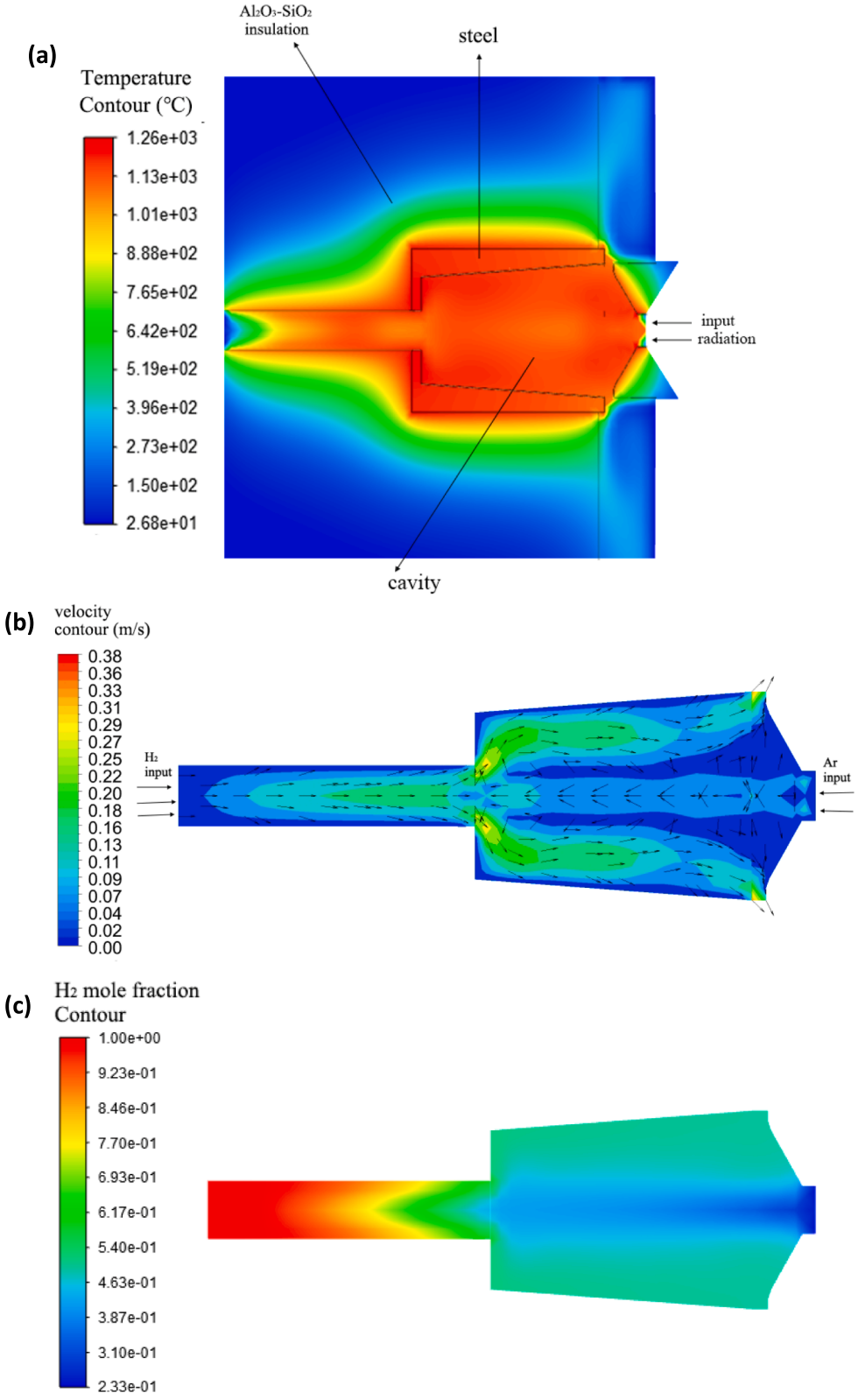

Fig. 3. Steady-state distribution profiles of (a) temperature, (b) gas velocity, and (c) H_2 mole fraction of the reactor 2D cross section.

The whole cavity is insulated by alumino-silicate fiber boards (poly-crystalline mullite/alumina wool, diameter 260 mm, length 200 mm) to reduce conductive heat losses, as shown in Fig. 1b.

As a variant, another cavity made of refractory ceramic was also tested to study the effect of the cavity material on the particle flowability and on the ore conversion at higher temperatures. The considered cavity has a smooth internal wall with a 3° tilt angle (inner diameters: 55 mm back and 65 mm front, outer diameter: 80 mm, length: 102 mm, volume: 289 cm^3). High-temperature resistant mullite material was selected (62 % Al_2O_3, 33 % SiO_2, 0.5 % Fe_2O_3, 0.5 % TiO_2, density 2.2 g/cm^3, 20 %

Table 2
Experimental conditions and results of the iron ore direct reduction with H_2 in the continuously-fed solar reactor using different cavities (Runs #1–4: stainless steel cavity, Runs #5–7: mullite cavity).

Run #	Iron ore particle size	Ar flow rate (NL/min) Inlet 1 + Inlet 2	H_2 inlet flow rate (NL/min)	T2 average value at steady state (°C)	Iron ore mass injected (g)	Mass of recovered iron product (g)	Theoretical H_2 consumption for complete Fe_2O_3 conversion (NL)	Actual H_2 consumed by the reaction (NL)	Conversion reached, α_{Fe2O3}	Total reaction duration (min)
1	1–2 mm	1 + 0.5	1	940	40	29.44	16.16	14.01	86.7 %	55.60
2	1–2 mm	1 + 0.5	1	930	30	21.26	12.12	11.04	91.1 %	62.32
3	<0.25 mm (powder)	1 + 0.5	1	920	39	24.55	15.76	14.95	94.9 %	67.28
4	1–2 mm	1 + 1	0.5	930	30	23.79	12.12	7.22	59.6 %	61.68
5	1–2 mm	1 + 0.5	1	1030	30	21.37	12.12	11.38	93.9 %	55.25
6	<0.25 mm (powder)	1 + 0.5	1	1040	39	26.06	15.76	15.10	95.9 %	68.82
7	1–2 mm	1 + 1	2	1020	31.9	20.56	12.92	12.91	99.9 %	42.85

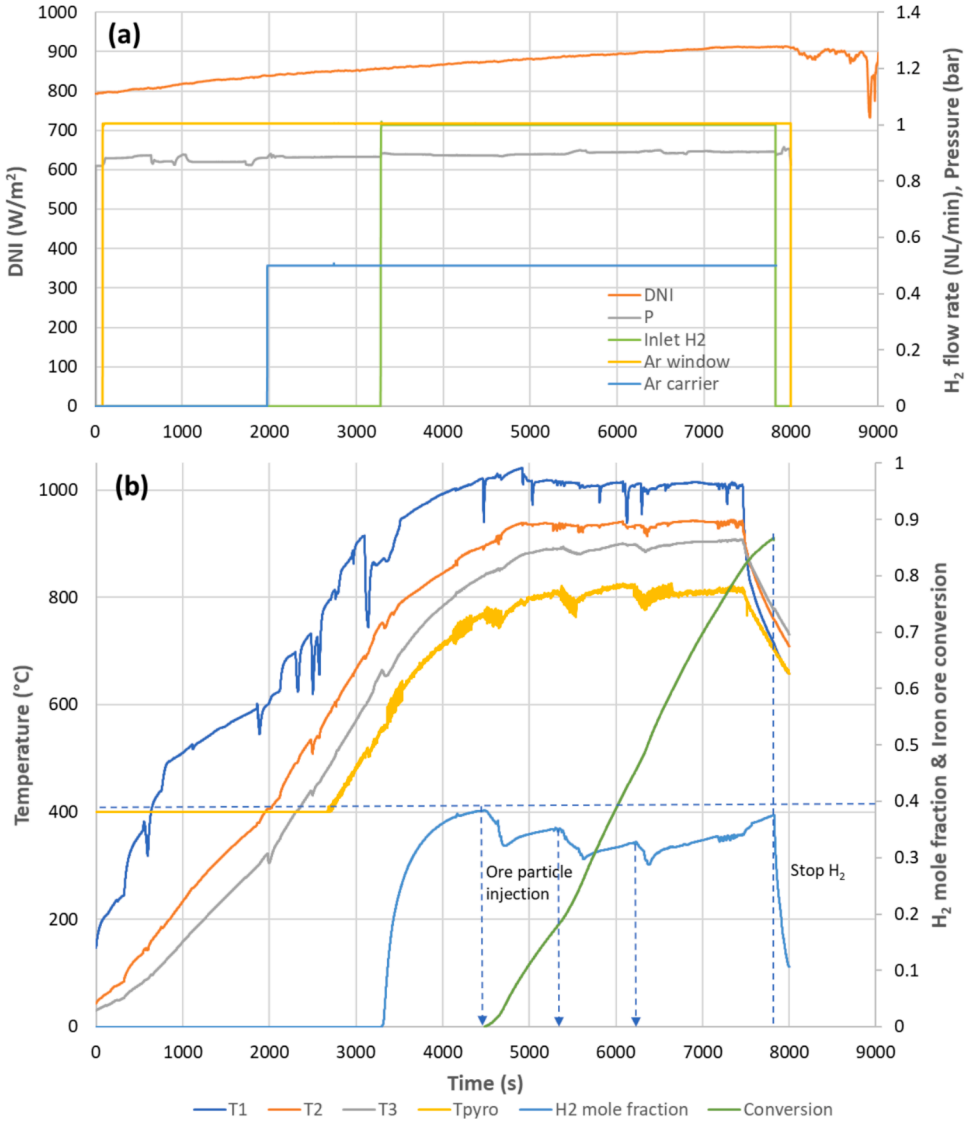

Fig. 4. Evolution of (a) DNI, reactor pressure, and gas flow rates, and (b) reactor temperatures, outlet H_2 mole fraction, and conversion during iron ore particles reduction with H_2 (Run #1: 40 g, 1–2 mm particle size).

open porosity, stable up to 1600 °C). Moreover, it is more resistant to thermal shocks than pure sintered alumina. The main expected benefit of using ceramics instead of the metallic cavity was to operate at higher temperatures to promote the reduction reaction kinetics.

The reactor chamber is closed at the front by a hemispherical transparent glass window to operate under controlled atmosphere. A

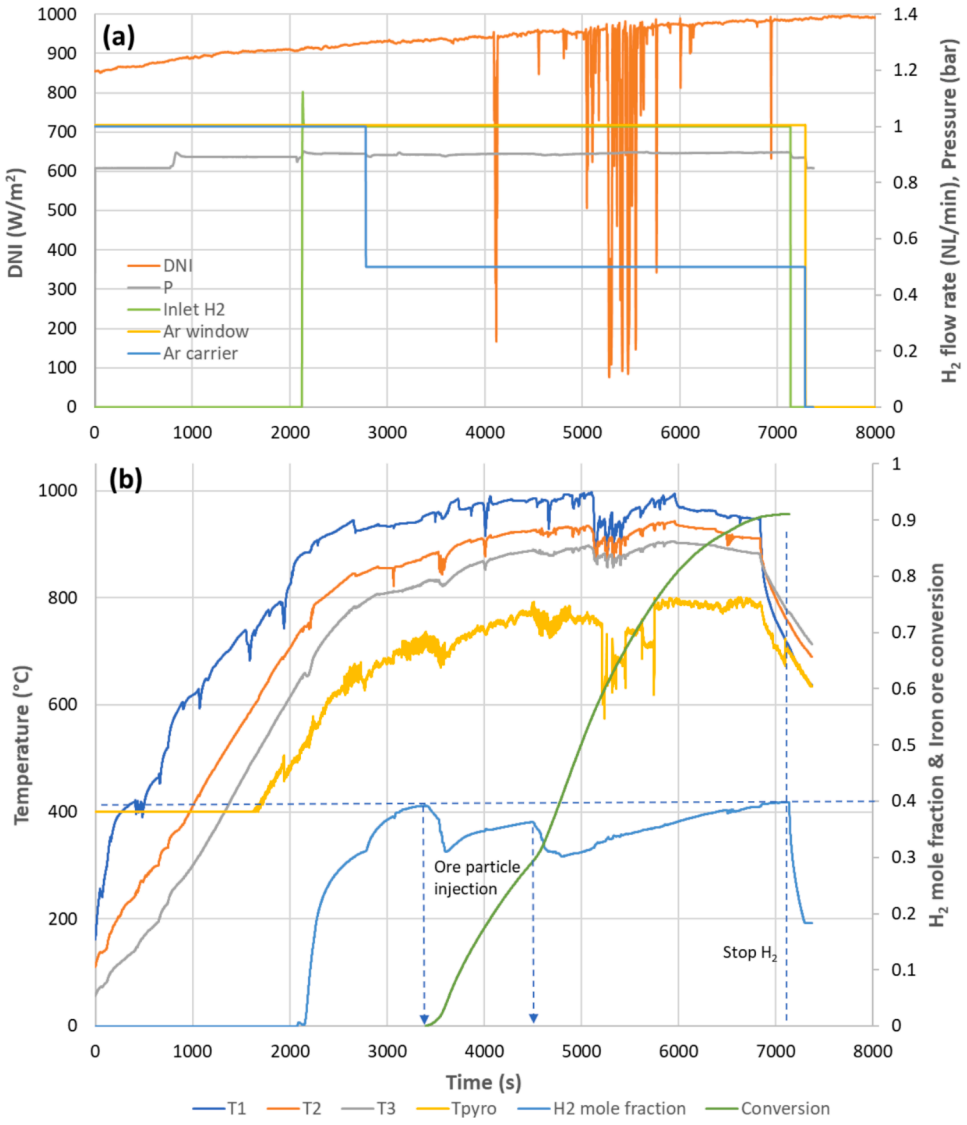

Fig. 5. Evolution of (a) DNI, reactor pressure, and gas flow rates, and (b) reactor temperatures, outlet H_2 mole fraction, and conversion during iron ore particles reduction with H_2 (Run #2: 30 g, 1–2 mm particle size).

flow of inert gas (Ar with ≥99.999 % purity, 1 NL/min) is injected through the window (via a gas inlet located at the front) to purge the window area. An additional Ar flow (0.5 NL/min) is injected upward from the reactor bottom to sweep the cavity exit zone and carry the produced steam toward the reactor outlet located at the top, as shown in Fig. 1b. The particle feeder is composed of a stainless-steel screw (diameters: 14x8 mm, step: 10.5 mm, length: 545 mm) and an airtight hopper (0.9 L) through which the reactive gas (H_2 with ≥99.9999 % purity) is injected (Fig. 1a). Hence, both the ore particles and H_2 enter together the cavity from the backside center. After exiting the cavity at the front side, the reacted particles fall by gravity inside a collection tank located underneath. The gas flow rates are regulated by mass-flow controllers (Brooks Instruments model SLA5850S, range: 0–2 NL/min, precision: ±0.2 % of full scale). The rotation of the cavity and of the screw feeder is ensured by two direct current motors with controllable rotational speed (depending on the applied voltage), and positioned at the rear of the reactor (Fig. 1a). Prior to experiments, a calibration of the motors was performed to adjust the residence time of particles in the cavity (fixed by the rotation speed of the cavity) and the feeding rate of particles (fixed by the rotation speed of the screw feeder).

The reactor is positioned at the focal point of a horizontal-axis solar furnace composed of a sun-tracking heliostat and a 2 m diameter parabolic concentrator (with 0.85 m focal distance), providing solar flux density with a Gaussian distribution and peak flux of 16 MW/m^2. The incident solar flux can be regulated thanks to a shutter positioned between the heliostat and the parabola, which is used to control the heating rates and the operating temperature in the reactor.

The reactor temperatures are measured by three type K thermocouples inserted from the backside of the cavity measuring the temperatures at three distinct locations (position of T1: 90 mm, T2: 55 mm, and T3: 10 mm from the back cavity wall). The thermocouple most exposed to solar radiation is shielded with an extra alumina protective sleeve and slightly bent (to be placed nearer to the wall and not at the cavity center axis). These thermocouples provide the temperature of the surrounding wall/solid due to thermal radiative equilibrium. In addition, an optical pyrometer (Heitronics KT15, 4.9–5.5 μm, range: 400–1900 °C, emissivity set to 1) is positioned at the reactor front and measures the temperature in the region around the tip of the screw exiting inside the cavity (through a CaF_2 window fixed at the top of the glass window). The reactor pressure is measured by different sensors (Keller PAA23, range 0–2 bar, accuracy: ±0.5 % of full scale), measuring the pressures inside the cavity and at the gas inlets/outlet (P1-P4).

The outlet gas flows through a condenser and a desiccant column to remove water formed by the reduction reaction, and the H_2

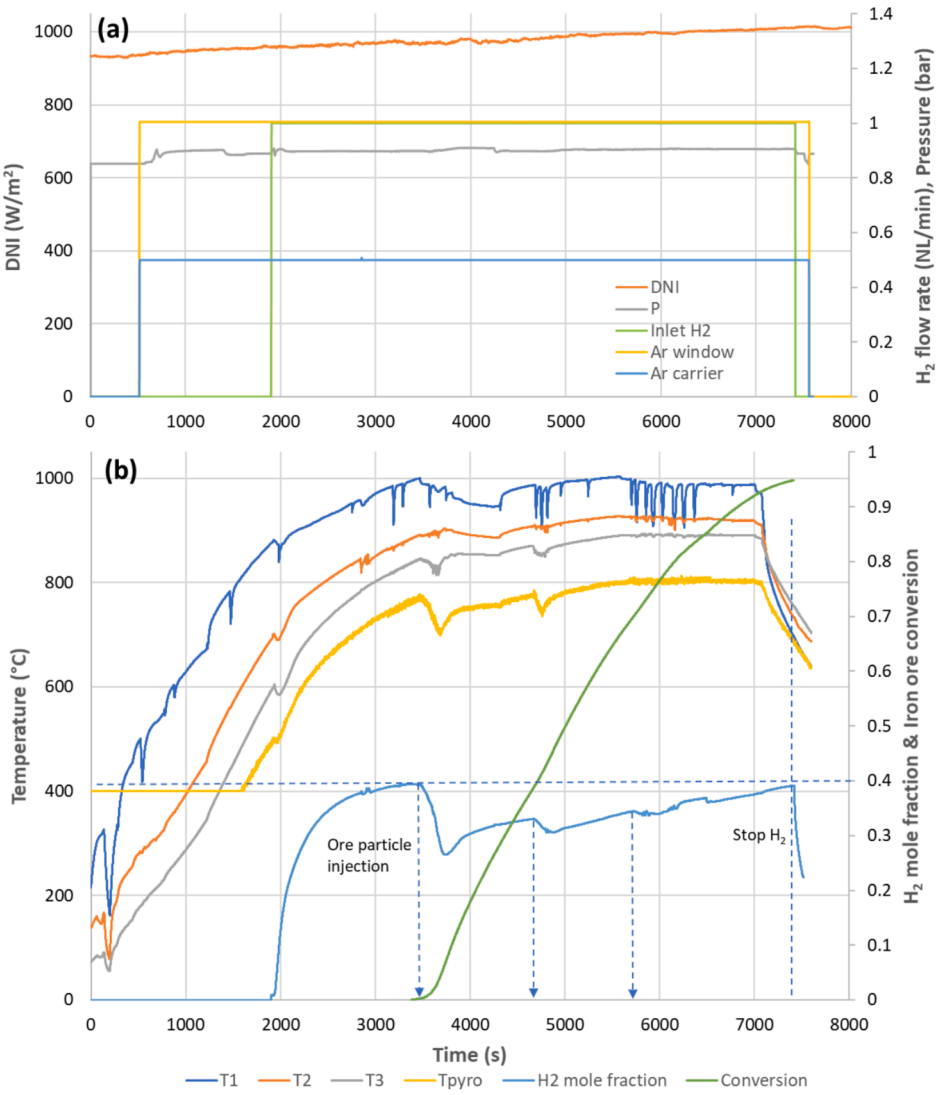

Fig. 6. Evolution of (a) DNI, reactor pressure, and gas flow rates, and (b) reactor temperatures, outlet H_2 mole fraction, and conversion during iron ore powder reduction with H_2 (Run #3: 39 g, <0.25 mm particle size).

concentration is then continuously measured by a gas analyzer (Emerson NGA2000) equipped with a thermal conductivity detector (scale: 0–50 %, precision: ±1 % of full scale). All the process parameters (gas flow rates, temperatures, pressures, gas concentrations) are recorded by a Beckhoff data acquisition system every 1 s.

2.2. Materials and methods

Solar experiments were carried out to investigate the performance of iron ore reduction and determine the oxide conversion during continuous solar operation, while analyzing online the evolution of outlet H_2 concentration to monitor the reaction progress. Fig. 2 illustrates the solar reactor operation during heating at the focus of the solar furnace, as well as the inside of the rotating cavity with progressing particles after their injection from the screw feeder.

To sum up the operating mode, the reactor was first solar heated without particles injection, then H_2 was added to reach the given concentration at the outlet. This allows checking that the inlet and outlet H_2 flow rates are equal. Once the outlet H_2 concentration was stable and equal to the inlet value (baseline), the iron ore particles were injected via the feeding system, with outlet gas analysis to precisely quantify the amount of H_2 consumed by the reaction (i.e., continuous monitoring of the oxygen removed from the oxide). The injection was done in several steps and the cavity rotation was stopped for periods to warrant long enough reaction duration. When the H_2 concentration reached back to the baseline value, the iron product was extracted by rotating the cavity. After reactor cooling, the iron product was recovered in the tank and remaining dust in the cavity was removed by vacuum cleaner. Such an operating mode was selected based on the high particle residence time required to approach complete conversion. With an upscaled reactor and higher cavity length, the particle residence time would be longer, which would favor the reaction completion. In this lab-scale reactor (with ~100 mm of cavity length), it was necessary to stop cavity rotation for a period to allow complete conversion before injecting new particles.

Iron ore pellets (supplied by ArcelorMittal) were used as a raw high-grade material containing the following main impurities (H_2O: 1.6 %, SiO_2: 1.68 %, Al_2O_3: 0.36 %, CaO: 0.58 %, MgO: 0.30 %, TiO_2: 0.15 %). The raw pellets (spherical granules of 10–15 mm size) were crushed and sieved in distinct size fractions to obtain the ranges of particle sizes used in this study (1–2 mm and <0.25 mm with bulk densities of 1.57 and 2.07 g/cm^3, respectively). For the raw powdered samples obtained after crushing, the particle size distribution was measured by laser diffraction analysis with dry dispersion method using a Malvern Mastersizer 3000 instrument. The powder showed the following granulometric characteristics: area-weighted mean diameter D[3,2] = 17.1 μm, volume-

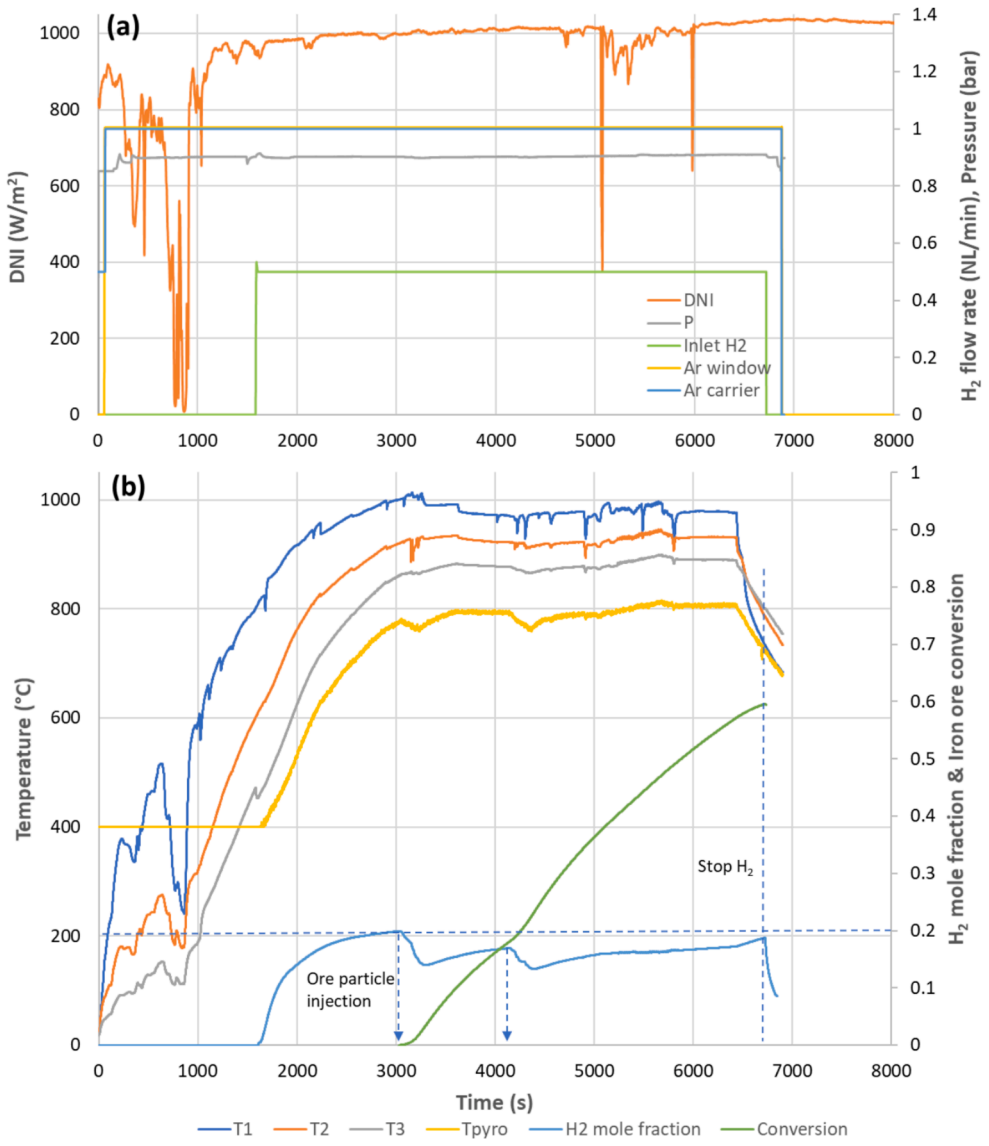

Fig. 7. Evolution of (a) DNI, reactor pressure, and gas flow rates, and (b) reactor temperatures, outlet H_2 mole fraction, and conversion during iron ore particles reduction with H_2 (Run #4: 30 g, 1–2 mm particle size, 0.5 NL/min H_2).

weighted mean diameter D[4,3] = 94.2 μm, median diameter Dv(50) = 66.0 μm, and 90th percentile diameter Dv(90) = 223.7 μm. The BET surface area (measured by N_2 adsorption at 77 K after degassing at 100 °C overnight) was 0.96 m^2/g for powder vs. 0.44 m^2/g for particles, and was mainly ascribed to the external surface because the materials are not porous. The mass fraction of Fe_2O_3 in iron ore was assumed to be 96 ± 1 wt% (confirming the percentage of impurities), based on direct reduction experiments by thermogravimetric analysis that was carried out to determine the reducibility potential of the raw material [30]. Prior to solar tests, a given mass of the raw iron ore was weighted (with ±0.001 g precision) and loaded in the hopper of the feeding system for injection in the reactor.

Powder X-Ray diffraction (XRD) analysis was performed on the fresh and reacted samples using a Panalytical X'PERT PRO diffractometer with the Cu Kα radiation (αCu = 0.15406 nm, angular range = 10–90°, 2θ, tube current 20 mA, potential 40 kV). The diffraction patterns were used to identify the main iron phases in the collected products and to assess the extent of ore reduction to metallic Fe. The morphology and microstructure of the materials were observed by Field Emission Scanning Electron Microscopy (FESEM – Zeiss sigma 300), completed by EDX analysis (Energy Dispersive X-ray Spectroscopy, Aztec EDX – Oxford Instruments, voltage of 15 kV) for elemental distribution.

The maximum iron oxide weight loss due to oxygen release, corresponding to a complete reduction of Fe_2O_3 to Fe, is expressed as:

$$m_{O,max}/m_{Fe_2O_3} = 3 \bullet M_O/M_{Fe_2O_3} = 30\% \quad (2)$$

where M_O and M_{Fe2O3} are the molecular weight (g/mol) of oxygen atom and Fe_2O_3, respectively, $m_{O,max}$ is the maximum mass of oxygen released from iron oxide, and m_{Fe2O3} is the initial oxide mass (g).

The iron oxide conversion was calculated by quantifying the amount of H_2 consumed by the reaction, based on the measured H_2 mole fraction at the reactor outlet for continuous reaction progress monitoring.

The time-dependent outlet H_2 flow rate (F_{H2}, NL/min at normal conditions 0 °C, 1 atm) was first determined from the outlet mole fraction (y_{H2}) and the total Ar flow rate (F_{Ar}):

$$F_{H_2,out} = F_{Ar} \bullet y_{H_2}/(1 - y_{H_2}) \quad (3)$$

The total mole amount of H_2 consumed by the reaction (corresponding to the difference between inlet and outlet H_2, integrated over the reaction duration) and the resulting Fe_2O_3 conversion were then calculated:

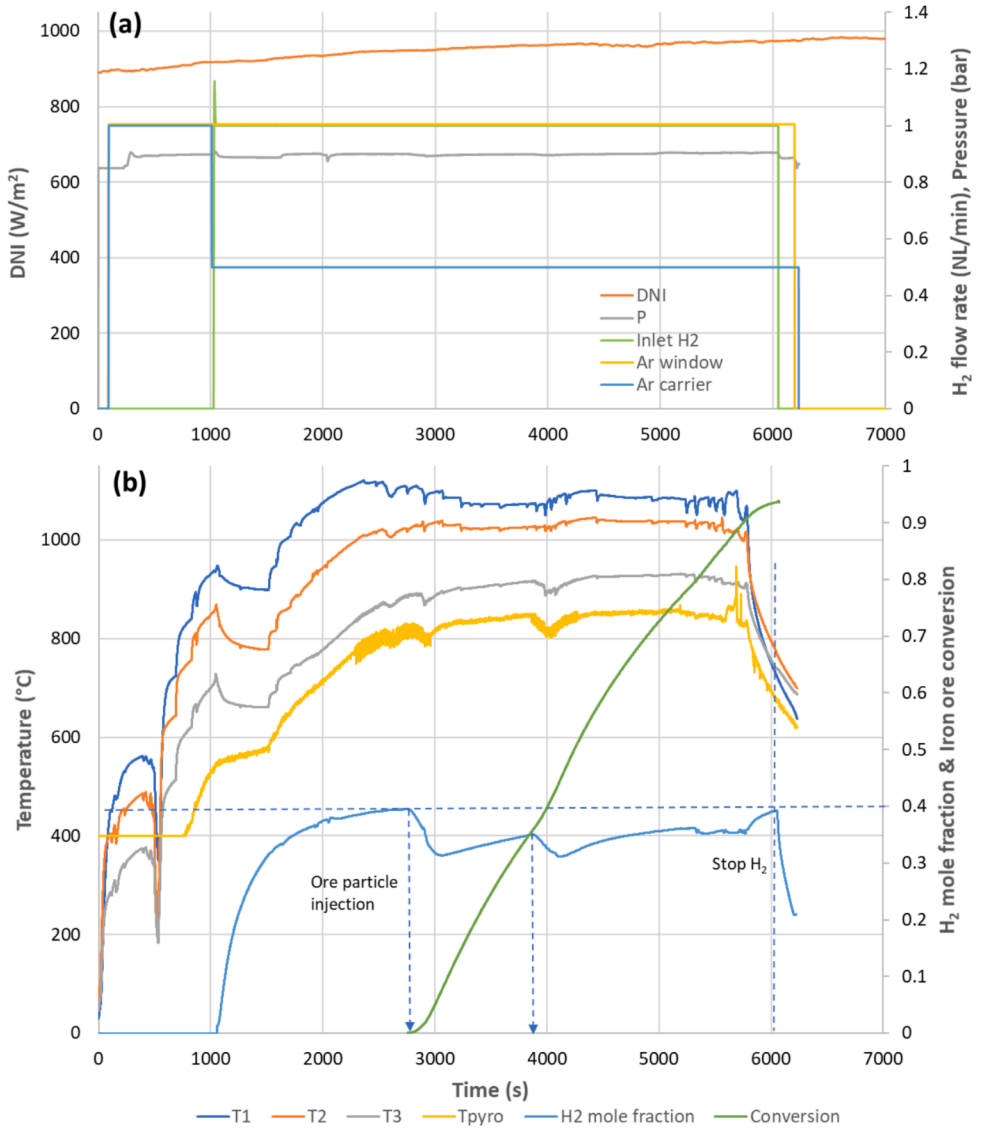

Fig. 8. Evolution of (a) DNI, reactor pressure, and gas flow rates, and (b) reactor temperatures, outlet H_2 mole fraction, and conversion during iron ore particles reduction with H_2 (Run #5: 30 g, 1–2 mm particle size).

$$n_{H_2} = \int_0^t (F_{H_2,in} - F_{H_2,out})/V_m \bullet dt \tag{4}$$

$$\alpha_{Fe_2O_3} = n_{H_2}/3n_{Fe_2O_3} \tag{5}$$

with n_{H2}: total amount of H_2 consumed by the reaction (mol), V_m: molar volume (22.4 L/mol at 0 °C, 1 atm), $n_{Fe_2O_3}$: initial mole amount of Fe_2O_3 (mol), $\alpha_{Fe_2O_3}$:Fe_2O_3 conversion.

3. Results and discussion

3.1. Preliminary CFD simulation of the solar reactor

Computational Fluid Dynamics (CFD) modelling was used for simulation of solar reactor operation and design validation. A 2D axisymmetric model (Ansys Fluent) was developed including coupled fluid flow, heat and mass transfer to determine the steady-state temperature distribution and gas velocity profile in the reaction chamber. The particle flow and chemical reaction were not included. Such thermal simulations were carried out chiefly to validate the cavity dimensions to reach the targeted reaction temperature with the available solar power input of the concentrating system.

The initial mesh was designed by the ICEM software and was composed of 2055 cells, 4825 faces, and 2287 nodes (maximum mesh size: 0.858 cm and minimum size: 0.0971 cm, using quad dominant type mesh). A solar flux density with Gaussian distribution is specified at the front aperture:

$$f(r) = F_1 \cdot e^{-(\frac{r-r_0}{\mu})^2} \tag{6}$$

where F_1 is the peak radiative flux at 10551 kW m^{-2}, r_0 is the position correction coefficient, r is the position, and μ is the standard deviation. The fitting parameter of r_0 is 0 (indicating that the concentrated radiation is maximum at the aperture center) and the fitting value of μ is 0.0048. This radiative flux is considered as a semi-transparent boundary condition and a diffuse radiation source (no directional characteristics) is assumed entering the blackbody-like cavity receiver. Regarding the external wall boundary, the outer reactor wall is subjected to convection and radiation exchanges with the environment at room temperature. Coupled conditions for interface boundaries are applied to every internal wall inside the reactor. The emissivity of the internal gas–solid coupled walls (stainless steel) is set at 0.7. Concerning the gas inlets (Ar at the front aperture and H_2 at the central tube also used to inject

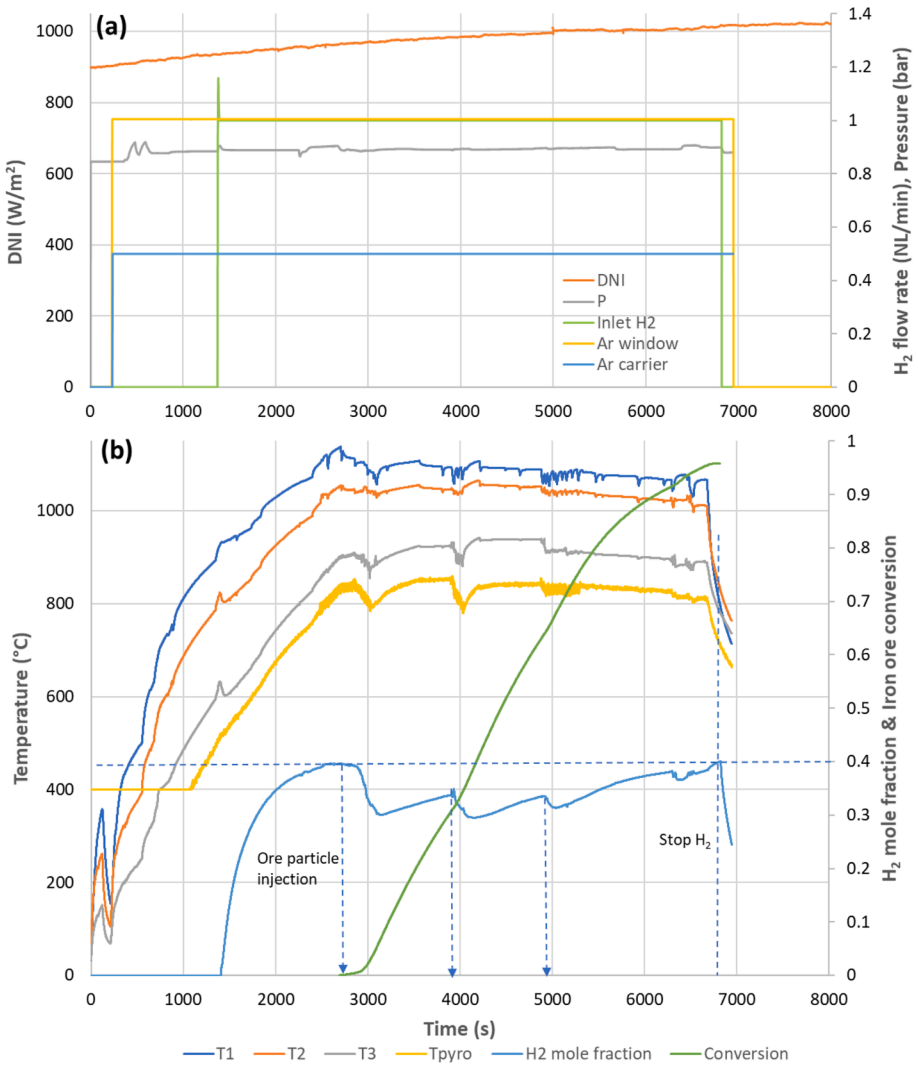

Fig. 9. Evolution of (a) DNI, reactor pressure, and gas flow rates, and (b) reactor temperatures, outlet H_2 mole fraction, and conversion during iron ore powder reduction with H_2 (Run #6: 39 g, <0.25 mm particle size).

particles), a mass flow inlet condition is specified. The set flow rate is $1.5{\cdot}10^{-6}$ kg s^{-1} (1 NL/min) for injected H_2 and $3{\cdot}10^{-5}$ kg s^{-1} (1 NL/min) for Ar. At the outlet, the condition of pressure outlet is specified. The flow regime in the reactor is laminar and the incompressible ideal gas model is applied for the gas density determination. A mixture of species (Ar, H_2) is considered in the flow and the mass diffusion of mixture gases is controlled by the species transport model. The species transport equations allow to compute the local mass fraction of each species, through the solution of a convection–diffusion equation for each species. Physical properties of materials are listed in Table 1. The model solves the coupled momentum, energy, radiation, and mass transport equations [47]. The radiative heat transfer is treated using the Discrete Ordinates (DO) radiation model. A mesh independence checking was carried out beforehand to warrant that the selected mesh was sufficient to provide stable and independent results. The cell number was increased from 2055 to 8220 and 32,880 cells, as shown in Fig. S1 (Supplementary Material). The mesh was refined in the cavity whereas a coarser mesh was used for the solid insulation parts. In Fig. S2, the temperature was plotted as a function of the distance along the symmetry axis between x = 0 at the backside (H_2 inlet) and x = 0.23 m at the front aperture. The steady state temperature at a monitor point (located at the center of the reactor cavity at x = 0.16 m) for the three mesh sizes was 1086 °C, 1100 °C, and 1084 °C respectively, thus representing a low variation of about 15 °C (temperature difference remaining below 1.4 %). The temperature profile along the reactor axis (Fig. S2) was not drastically influenced by the mesh size, especially in the cavity zone (between x = 0.12 and 0.20 m).

The temperature contour, shown in Fig. 3a, reveals a relatively homogeneous temperature distribution inside the cavity (1000–1150 °C), and the efficient role of the insulating zone keeping the outer reactor walls at low temperature. The maximum temperature of the metallic cavity reaches 1260 °C for the available solar power input, thus appropriate for the DRI reaction. The Ar flow from the front aperture enters the cavity toward the back as shown by the gas velocity contour (Fig. 3b), and the H_2 molar fraction within the cavity near the walls is close to 0.5 (Fig. 3c). These simulations confirmed the suitability of the reactor design and cavity size for uniform heating of the whole reaction zone while reaching the required reaction temperatures.

Future simulations will be used to optimize the reactor design and geometry with reactive particles as well as the operating conditions (solar concentration/flux density, solar power input, reactant feed rate, etc.). A special attention will be paid on the reactor design to achieve both limited and controlled thermal gradients in the reaction chamber and maximum solid residence time for ensuring complete ore conversion and selective production of iron.

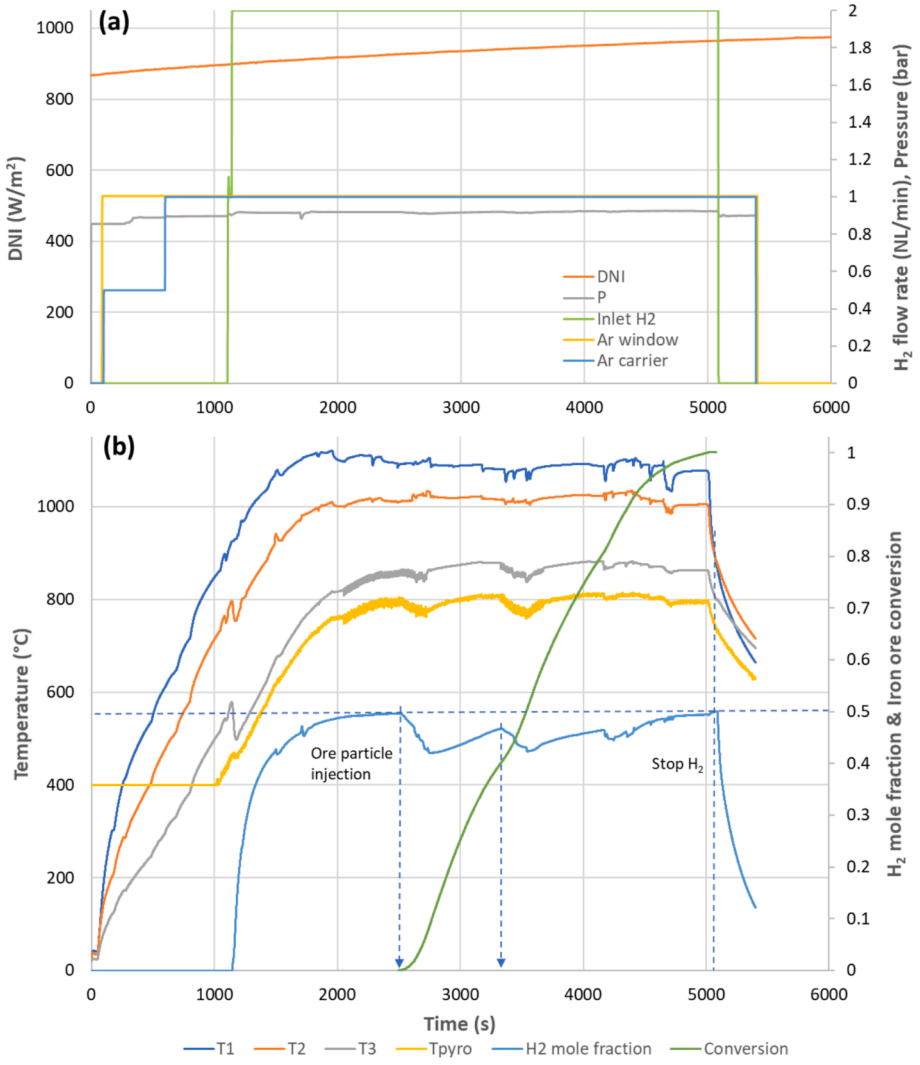

Fig. 10. Evolution of (a) DNI, reactor pressure, and gas flow rates, and (b) reactor temperatures, outlet H_2 mole fraction, and conversion during iron ore particles reduction with H_2 (Run #7: 31.9 g, 1–2 mm particle size, 2 NL/min H_2).

3.2. Solar reactor testing and experimental performance analysis

This section is related to the on-sun testing and analysis of the solar reactor performance. Different solar experiments were carried out to optimize the reduction extent and to investigate chiefly the effect of particle size (mm-scale particles vs. μm-scale powder), gas flow rates, and type of cavity on the global reactor performance and particle conversion. The outlet gas composition was measured continuously to determine the conversion and the recovered solid iron products were also characterized (by XRD and SEM/EDX). Table 2 summarizes the main experimental conditions and results of the direct reduction of iron ore with H_2 in the solar reactor. On the basis of the combined uncertainties on the H_2 mole fraction analysis, gas flow rate, and initial iron ore mass, the maximum relative uncertainty on the calculated chemical conversion α_{Fe2O3} (Eq. (5)) is ±1.5 %.

3.2.1. Iron ore solar reduction in the metallic cavity

In Run #1, a total of 40 g (±0.001 g) of iron ore (1–2 mm particle size) was loaded in the particle feeder and the feeding was split in three stages (corresponding to ~13.3 g injected during each stage). Fig. 4 shows the evolution of the different measured data (Direct Normal Irradiation DNI, gas flow rates, cavity pressure, temperatures, and H_2 mole fraction). The heating period of the solar reactor was over ~1 h. The cavity temperature showed a temperature gradient between the irradiated front and the rear (maximum values measured at T1 at the cavity front), and the temperature difference between T1 and T3 was about 100 °C (±10 °C) at thermal equilibrium (due to the thermal gradient in the axial direction because the solar radiation entered from the front face of the cavity). The measured temperatures at T1 and T3 were ~1000 °C and 900 °C. A lower temperature of about 800 °C was measured at the screw feeder tip by the pyrometer (T_{pyro}), likely due to an underestimation because the emissivity was set to one. Actually, the real temperature value in this zone thus lied between the measured temperatures of T_{pyro} and T3. The control temperature was taken at T2 (~940 °C) located in the central zone of the cavity. The solar power applied to reach these cavity temperatures was in the range 1300–1400 W.

H_2 was first injected alone in the cavity before iron ore particle injection in order to establish the baseline used for quantifying the amount of H_2 consumed by the reaction and the conversion (Eqs. 4–5). The amount of H_2 consumed corresponded to the area between the baseline and the curve of H_2 measured during reaction. A step-increase of the H_2 input flow rate resulted in a slow response of the H_2 signal at the reactor outlet after the step H_2 injection due to the high reactor volume (~20–25 min needed to reach the nominal outlet H_2 concentration). Once the H_2 concentration at the reactor outlet reached the nominal value (40 %), the particle feeding was started (at 4.2 g/min feeding rate during ~190 s) with a temperature in the cavity front above 1000 °C

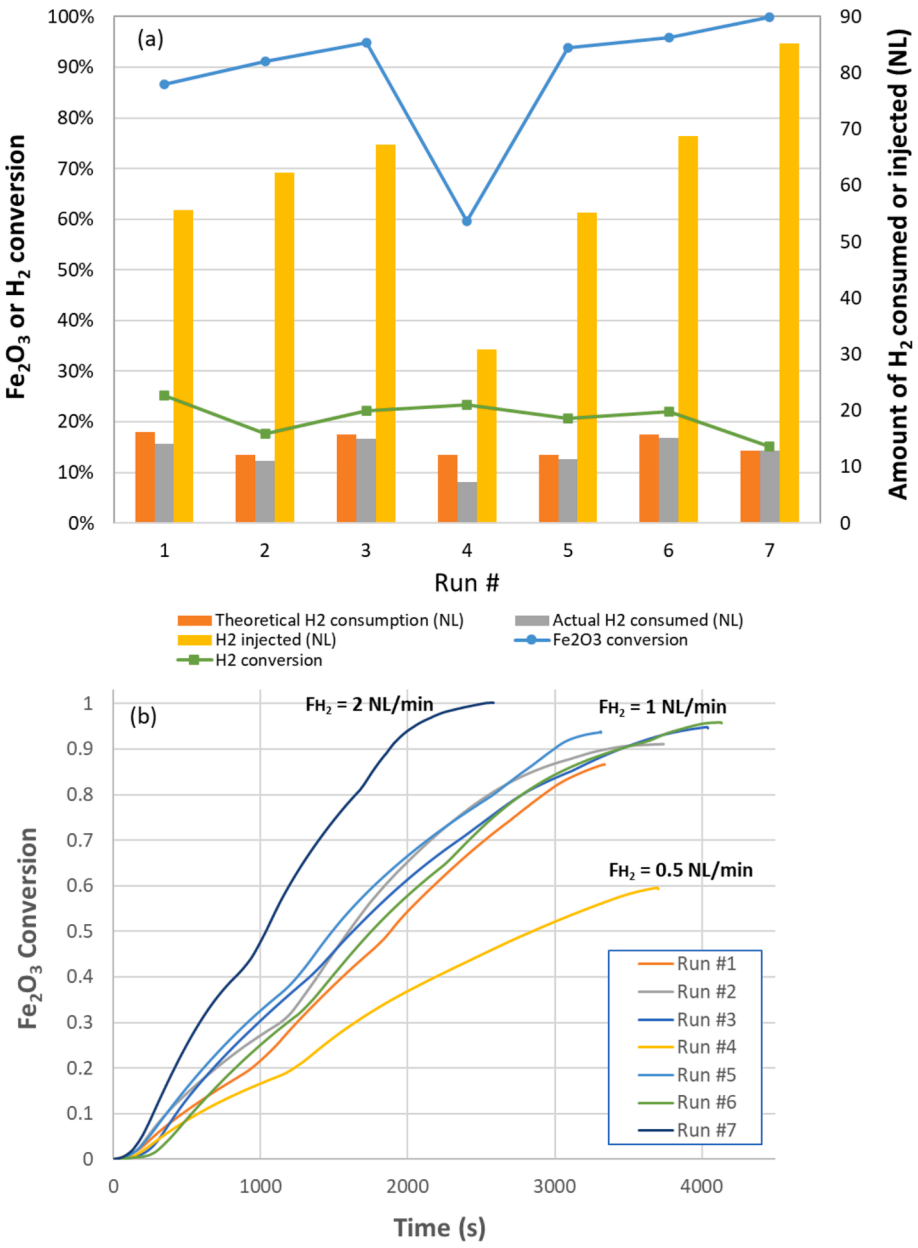

Fig. 11. (a) Total amounts of H_2 consumed/injected, and conversion of Fe_2O_3 and H_2 for Runs #1–7. (b) Evolution of Fe_2O_3 conversion showing the prevailing effect of H_2 flow rate on the reduction rate.

(T1). The feeding duration was fixed to inject ~13.3 g in the cavity. Simultaneously, after periods of 30 s, the cavity was rotated during 30 s sequentially twice (total rotation time: 1 min at 4.8 rpm – round per minute), to homogenize the particles along the cavity length. This ensured a more even distribution of the particles while ensuring they were not removed from the cavity since the residence time of particles in the cavity would be about 80 s with a cavity rotation at 4.8 rpm (which is the minimum rotation speed given by the motor). To ensure longer residence times and high enough reaction duration, the cavity rotation was thus stopped to keep the particles in the hot cavity as long as the reaction was still in progress, as monitored by the outlet H_2 gas analysis.

As soon as the particles entered the heated cavity, the outlet H_2 mole fraction started to decrease. Then, the injection was stopped and the reactor was maintained under stable conditions during 10 min (without rotation), which resulted in the increase of the H_2 concentration during the progress of the reduction reaction. The same procedure was further repeated twice to complete the particle load injection. Finally, the last step consisted in waiting that the H_2 mole fraction increased to approach its nominal value (40 %), which witnessed that the reaction approached completion. However, this last step was not fully reached, which resulted in a final conversion of ~87 % after 55.6 min of reaction. The reaction was thus not fully completed when H_2 was stopped. The obtained conversion corresponded to 14.01 NL of H_2 consumed by the reduction reaction to remove oxygen from Fe_2O_3 (16.16 NL theoretically required for a full conversion). Accordingly, the mass of recovered Fe products was lower compared to the initial iron ore mass injected (Table 2), due to the loss of oxygen (a complete Fe_2O_3 reduction to Fe would correspond to about 30 % of mass loss according to Eq. (2)).

The objective of the next runs was then to enhance the iron ore conversion. The amount of loaded iron ore was lowered to 30 g in Run #2 and the other conditions were kept identical to Run #1. All the recorded measurements and conversion results are illustrated in Fig. 5. The heating duration of the solar reactor was shortened to around 45 min. The particle feeding period was divided in two stages (each with 15

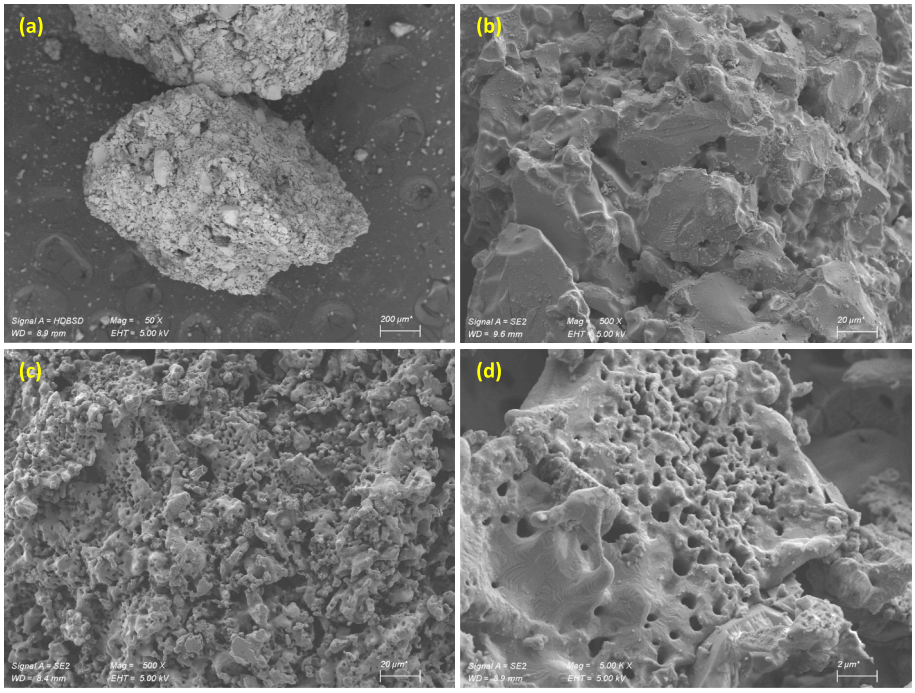

Fig. 12. FESEM analysis of (a,b) raw iron ore particles and (c,d) collected Fe products (Run #7).

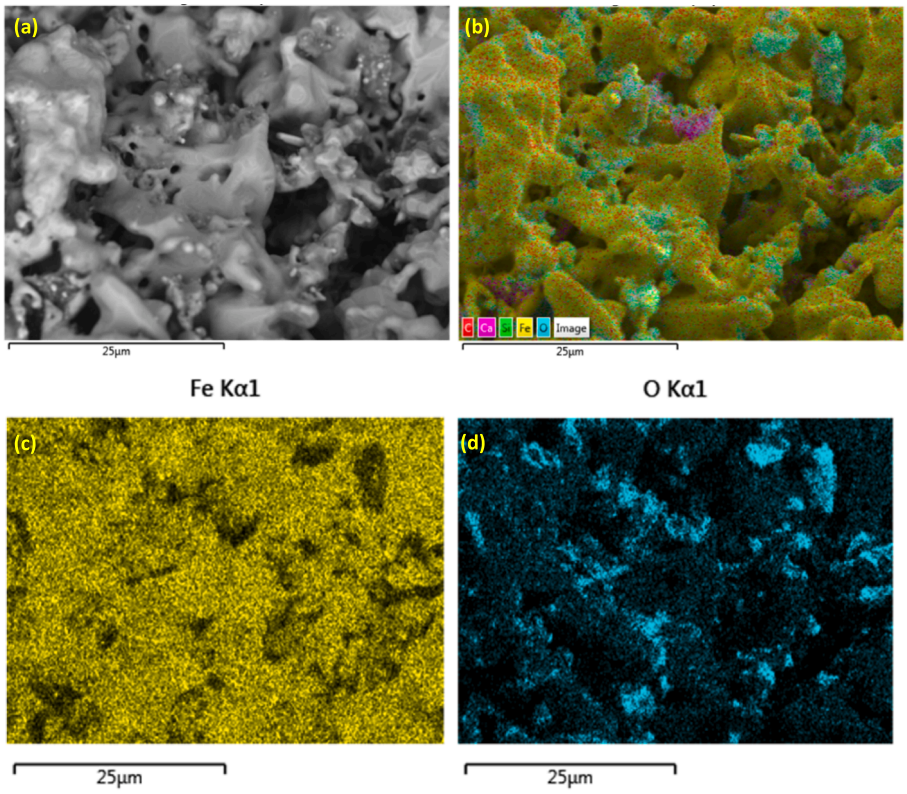

Fig. 13. FESEM image and EDX mapping of iron particles obtained in Run #7.

g fed during ~214 s, waiting time: 16 min in 1st stage, 44 min in 2nd stage) and the final waiting time after the second injection period was long enough to ensure that the H_2 concentration returned to the initial value, so that the reaction approached completion after about 1 h. The much longer duration of the 2nd stage was also partly due to sharp variations of the solar DNI due to passing clouds, causing instabilities and temperature drops. As a result, a final calculated conversion of ~91 % was reached based on the total amount of H_2 consumed (11.04 NL versus 12.12 NL of H_2 required for a complete conversion).

3.2.2. *Influence of particle size and H_2 flow rate on conversion*

The effect of the size of iron ore particles on the reaction extent was

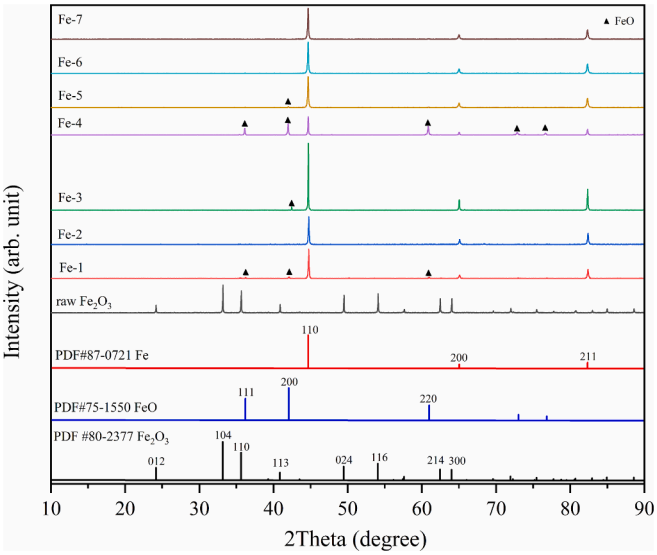

Fig. 14. XRD analysis of raw iron ore and collected Fe products (Runs #1 to #7) after reduction in the solar reactor.

investigated in Run #3 (Fig. 6). Iron ore powder (40 g) was used instead of particles, while keeping the same operating conditions as in previous runs with T2 of about 900–925 °C. The particle size after sieving was below 0.25 mm and such a powder contained a mix of the finest crushed particles and dust, with an external surface area inversely proportional to the diameter. The injection period was divided in three stages (13.3 g each) and the final conversion reached about 95 % after stopping the H_2 injection (14.95 NL of H_2 consumed), once the H_2 mole fraction approached its initial value. It can be concluded that the fine ore particles promote the reduction reaction due to a higher external surface, since the final conversion is slightly enhanced in comparison to Run #1, although the time to reach maximum conversion is globally unchanged (about 1 h).

Finally, the effect of the H_2 flow rate on the reactor performance was studied in Run #4 by considering half of the H_2 flow rate of Run #2 (0.5 NL/min instead of 1 NL/min). Fig. 7 shows the time evolution of all the measured data and iron ore conversion. The total Ar flow rate injected at the reactor front inlets was 2 NL/min. The outlet H_2 concentration was thus 20 % at the baseline and two injection periods were settled (15 g fed during 214 s in each stage and cavity rotation twice during 30 s). The final conversion reached about 60 % after one hour of reaction, which definitely confirms that a lower H_2 flow rate drastically decreased the reaction extent. A longer reaction duration would thus be required to enhance the final conversion. Actually, based on the amount of iron ore fed (30 g), the theoretical amount of H_2 required for complete reduction can be calculated (corresponding to 3 times the amount of Fe_2O_3 based on the reaction stoichiometry). This equates to 12.12 NL of H_2 consumed for a complete Fe_2O_3 reduction (whereas only 7.22 NL of H_2 was consumed by the reaction in this run). It is thus normal that increasing the inlet H_2 flow rate favors the reduction extent as it favors the mass transfer rate of reacting gas to the reaction site and the diffusion of H_2 gas in the layer of solid particles. Moreover, increasing the H_2 mole fraction was also shown to enhance drastically the rate of the reduction reaction [30]. Although pure H_2 was fed from the cavity back through the screw path together with the solid particles, it is likely that some dilution occurred in the cavity space with the inert Ar gas flows injected from the reactor front, as evidenced by CFD simulation (Fig. 3c).

It can be concluded that a large excess of H_2 is beneficial for the reaction conversion. Therefore, the use of large H_2 flow rates is necessary to favor the reduction reaction, which entails a large amount of unconverted H_2 at the reactor outlet. In an industrial process, H_2 recovery and recycling should be considered to warrant the full consumption of H_2, which can be simply achieved by condensing the outlet water steam and reinjecting the unconverted H_2 to the reactor inlet.

3.2.3. *Iron ore solar reduction in the ceramic cavity*

High temperature operation brings challenges for the long-term thermal and chemical stability of reactor materials, due to thermo-mechanical resistance issues, heating/cooling stages, and reducing gas atmosphere. Thus, a refractory ceramic cavity was considered instead of the metallic cavity to withstand higher temperatures. Accordingly, suitable materials should be selected based on different criteria (maximum operating temperature, resistance to thermal shocks, chemical inertness / compatibility, thermal conductivity and radiative properties). It must be noted that the previously used metallic cavity remained intact after the series of solar experiments conducted (Runs #1–4) without any chemical interaction with the oxide, although the iron product tended to adhere to the cavity wall.

A cavity made of mullite was used in Run #5 with lower internal diameters to operate at higher temperatures. Increasing the temperature was shown to speed up the reduction rate [9], although the formation of a denser γ-Fe phase (above 912 °C) may slow down the kinetics between 900 and 1100 °C due to solid-state diffusion limitation [49]. Fig. 8 confirms that temperatures over 1000 °C were reached at T2 (~1020–1040 °C), while T1 was close to 1100 °C with a constant temperature gap of ~50–60 °C between T1 and T2. The temperature gap between T2 and T3 was about 110 °C, which means that T3 at the cavity rear was at a slightly higher temperature (~920–930 °C) than in previous runs with the metallic cavity. The maximum value of T_{pyro} was ~ 850 °C, thus 50 °C higher than in previous runs. The mullite cavity thus exhibits much higher temperatures in the front zone, but the temperature gradient in the axial direction is more pronounced because of the lower thermal conductivity of ceramics (1.5 W/m.K for mullite vs. 14–16.3 W/m.K for AISI type 304L stainless steel). The solar power to reach these temperatures was in the range 950–1000 W. It has to be noted that the required power to heat the mullite cavity was much lower than in the case of the stainless-steel cavity due to the lower cavity dimensions and internal volume. The heating duration was also significantly reduced (less than 30 min). The mullite cavity remained intact with no impact of solar heating on the material stability, given that the operating temperatures were much below the maximum temperature allowed for this material (~1600 °C).

The particle injection was started once the H_2 concentration reached 40 %. The feeding period was divided in two stages as in Run #2 (each with 15 g fed during ~214 s, waiting time: 16 min in 1st stage, 37 min in 2nd stage) and the cavity was rotated 30 s at 4.8 rpm with 10 s stepwise in order to ensure particle spreading and motion toward the cavity front. As a result, after a total reaction duration of 55 min, the conversion reached almost 94 % (with a total consumption of H_2 by the reduction reaction of 11.38 NL), which is higher than in Run #2 carried out with the same conditions.

The same ceramic cavity and heating conditions were applied in Run #6 with ore powder (for a comparison with Run #3 held at lower temperatures in the metallic cavity). The heating duration was about 40 min and T2 temperature was in the range 1030–1050 °C when the reaction was carried out (Fig. 9). The feedstock injection was divided in three stages (13.3 g each). A final conversion of 95.9 % was reached (corresponding to 15.10 NL of H_2 consumed), thus slightly higher than in Run #5 (with larger particle size) and similar to Run #3. Therefore, the effect of particle size was confirmed, with a slightly higher conversion for the powder whatever the temperature (Run #2 vs. Run #3 and Run #5 vs. Run #6 in Table 2). Globally, the total reaction time also remained unchanged (although the temperature was 100–150 °C higher than in Run #3). Basically, the reaction duration varied depending on the amount of reactant injected in the cavity (the reaction is slightly longer when injecting a higher particle mass in Runs #3 and #6, and the reaction rate is limited when the H_2 flow rate is decreased in Run #4).

Therefore, the kinetic rate was mainly controlled by the H_2 reducer feeding rate as the main limiting factor, rather than being controlled by the temperature.

The ultimate test, shown in Fig. 10, was carried out with increasing the H_2 flow rate to 2 NL/min (Run #7) to assess its favorable impact on the particle conversion. The H_2 concentration before iron ore injection was 50 % and the temperature was kept identical to previous Runs #5 and #6 (T1 ~ 880 °C, T2 ~ 1020 °C, and T3 ~ 1090 °C). In this case, the conversion reached about 100 % and the time to reach reaction completion was much reduced (~43 min), which confirms that increasing the H_2 flow rate strongly promotes the reduction rate.

Fig. 11a summarizes the experimental data regarding the amounts of H_2 consumed/injected, and the resulting global Fe_2O_3 and H_2 conversion (Fe_2O_3 conversion: ratio of H_2 consumed to theoretical H_2 consumption (Table 2), H_2 conversion: ratio of H_2 consumed to the amount of H_2 injected during the reaction period). The amount of injected H_2 varies in the range of 55.6–68.7 NL except in Run #4 (30.8 NL) and #7 (85.2 NL) due to the different inlet H_2 flow rates. As a result, the H_2 conversion varies in the range 15.2–25.2 % and it is the lowest in Run #7 due to the highest H_2 flow rate injected.

A summary of the effect of H_2 flow rate on particle conversion is illustrated in Fig. 11b gathering all the experimental conversion results. Increasing the H_2 flow rate significantly enhanced the reduction rate and the final Fe_2O_3 conversion. This confirms that an excess of H_2 is required to hasten the reduction reaction and to favor complete conversion. This suggests that a high H_2 flow rate favors the gas diffusion in the solid particle layer, and further shifts the equilibrium toward product formation while diluting the steam product. This flow rate effect indicates that the rate limiting step is likely related to gas diffusion.

The limitation of the current reactor design is related to the short cavity length (~100 mm long) that would need to be increased to enhance the particle residence time. Therefore, the cavity rotation was stopped for periods to increase the reaction duration and allow for complete conversion. This is a way adopted to warrant that the particles have sufficient time for the reaction with H_2. With an upscaled reactor and higher cavity length, the particle residence time would be longer, which would favour the reaction completion.

Solar tests showed that the conversion process under H_2 flow is slow even at cavity temperatures above 1000 °C. The control of the particle residence time in the heated zone of the solar reactor was identified to be important [30]. A high residence time at high temperature is crucial for the process, although not being a sufficient condition for warranting the complete particle conversion. The H_2 reactant also plays a key role. Indeed, it was also previously highlighted that a large H_2 excess (with respect to reaction stoichiometry) is necessary to favour the reaction toward Fe product [7,30]. In this work, H_2 was fed at only 1 NL/min in most runs (to avoid overconsumption) and the conversion of 30 g iron ore theoretically requires the consumption of 12.12 NL H_2, which would translate in a minimum reaction duration of ~12 min (provided that all the injected H_2 could react with Fe_2O_3, which is not possible as most part of the H_2 flows out of the reactor and is unconverted: 43.8 NL outlet H_2 in Run #5 for 55.2 NL injected). This therefore explains why much higher reaction durations were required in practice to convert the iron ore feedstock. Then, optimized gas and solid flow patterns are required to enhance the solid–gas reaction. In future works, the reactor modelling will be a first tool to optimize the reactant feeding rate as a function of the reactor geometry and dimensions. The solid residence time will also need to be experimentally varied to optimize particle conversion and Fe yield as a function of the operating temperature and H_2 flow rate.

3.2.4. Solid products analysis

SEM analysis shows dense non porous raw ore particles (Fig. 12a,b), whereas the reduced product features a porous microstructure that is characteristic of sponge iron (pore diameter below 1 μm) with surrounding sintered zones (Fig. 12c,d). EDX mapping confirms the homogeneous distribution of Fe element (Fig. 13), whereas O is more located in zones where Fe is lacking and overlaps with impurities such as Ca and Si (suggesting the presence of the corresponding oxides).

The collected products were also analyzed by XRD to determine their purity/phase composition (iron content). For all the samples shown in Fig. 14, the main phase was Fe (PDF 87-0721). In Run #4, the material reduced with 0.5 NL/min H_2 also contained wuestite FeO (PDF 75-1550), in agreement with the lowest conversion (~60 %) measured in this run. The presence of Fe_2O_3 or Fe_3O_4 was not detected in the solar-reduced samples, whereas minor peaks attributed to non-stoichiometric wuestite phase ($Fe_{1-y}O$) intermediate product were only identified in Runs #1 and #3. Hence, these solid products XRD analyses confirmed the formation of a pure Fe phase from raw iron ore in the rotary solar reactor. The feasibility of pure Fe production via solar-driven H_2-DRI was thus demonstrated through identification of the product composition.

This approach totally eliminates the direct CO_2 emissions of conventional processes based on coal/char reduction or syngas-based DRI. A life cycle analysis will be required to assess the global environmental impact of the whole process chain including solar facilities construction (tower and heliostat field), iron ore extraction/transport, and H_2 reducer production. Associated supply costs of feedstocks must also be included (in addition to the capital cost of the solar concentrating system) when evaluating the economic feasibility of a large-scale solar plant for iron production.

4. Conclusion

The objective of this study was to experimentally demonstrate the feasibility of direct reduced iron under H_2 atmosphere in a novel rotary-type solar reactor. The developed reactor prototype offered a suitable solution for efficient solar heating of the reacting particles, iron ore particles injection in the solar-heated rotary cavity, and solid products recovery with reaction progress continuous monitoring. The reactor was first designed and simulated, before being experimentally tested on-sun for reliable operation validation and performance evaluation (such as the products yields as a function of the operating conditions). The influence of cavity temperature, iron ore particle size, flow rate of injected H_2 reducer, and type/size of cavity was unravelled. High iron ore conversion was achieved (up to 95 % for powder in the metallic cavity and 96 % in the ceramic cavity at 1 NL/min H_2), resulting in the production of a high-value Fe-rich solid product, as confirmed by the XRD characterization of the recovered materials. At lab-scale, the conversion rate was limited by the relatively low H_2 flow rate used (1 NL/min) thus requiring long duration to convert the whole feedstock, and by the low cavity size hindering the particle residence time. Increasing the H_2 flow rate (to 2 NL/min) enhanced the reduction rate significantly, with a final particle conversion of 100 %. Thereby, the reduction kinetics was mainly controlled by the feeding rate of the H_2 reducer rather than by the temperature. Thus, a large H_2 excess was recommended to hasten the reduction reaction and reduce the particle residence time, which in turn makes necessary the recycling of unconverted H_2 in a large-scale process.

The reduction process was successfully demonstrated in the solar-heated reactor, confirming the feasibility of renewable iron production from direct ore reduction, and thus paving the way toward decarbonation of the iron and steel metallurgical industry.

Future work will focus on the detailed reactor modelling including thermal, two-phase flow hydrodynamics, and chemical aspects (solid–gas reaction kinetics) for both design optimization and process extrapolation studies. The performance outputs including gas concentration distributions, particle conversion/Fe yield, and energy conversion efficiencies will be determined. The reactant feeding rate will also be optimized to match the rate of the chemical reaction, in order to obtain a suitable particle residence in the reaction chamber while reaching complete conversion.

CRediT authorship contribution statement

Stéphane Abanades: Writing – review & editing, Writing – original draft, Visualization, Validation, Supervision, Software, Resources, Project administration, Methodology, Investigation, Funding acquisition, Formal analysis, Data curation, Conceptualization. **Roger Garcia:** Resources, Conceptualization. **Jian Cong:** Visualization, Investigation, Formal analysis, Data curation.

Declaration of competing interest

The authors declare that they have no known competing financial interests or personal relationships that could have appeared to influence the work reported in this paper.

Acknowledgments

This work was funded by the French National Agency for Research (ANR, METASOL project, contract N° ANR-20-CE05-0008-02). The authors thank the materials characterization platform of PROMES (E. Bêche) for providing the XRD analysis equipment. ArcellorMittal is also gratefully acknowledged for supplying the raw iron ore pelletized material.

Appendix A. Supplementary data

Supplementary data to this article can be found online at https://doi.org/10.1016/j.cej.2025.159441.

Data availability

Data will be made available on request.

References

[1] C. Bataille, M. Åhman, K. Neuhoff, L.J. Nilsson, M. Fischedick, S. Lechtenböhmer, B. Solano-Rodriquez, A. Denis-Ryan, S. Stiebert, H. Waisman, O. Sartor, S. Rahbar, A review of technology and policy deep decarbonization pathway options for making energy-intensive industry production consistent with the Paris Agreement, J. Clean. Prod. 187 (2018) 960–973, https://doi.org/10.1016/j.jclepro.2018.03.107.

[2] M. Fischedick, J. Marzinkowski, P. Winzer, M. Weigel, Techno-economic evaluation of innovative steel production technologies, J. Clean. Prod. 84 (2014) 563–580, https://doi.org/10.1016/j.jclepro.2014.05.063.

[3] L. Holappa, A general vision for reduction of energy consumption and CO_2 emissions from the steel industry, Metals 10 (2020) 1117, https://doi.org/10.3390/met10091117.

[4] Z. Fan, S.J. Friedmann, Low-carbon production of iron and steel: technology options, economic assessment, and policy, Joule 5 (2021) 829–862, https://doi.org/10.1016/j.joule.2021.02.018.

[5] F. Patisson, O. Mirgaux, Hydrogen ironmaking: how it works, Metals 10 (2020) 922, https://doi.org/10.3390/met10070922.

[6] D. Wagner, O. Devisme, F. Patisson, D. Ablitzer. A Laboratory Study of the Reduction of Iron Oxides by Hydrogen, in: Advanced Processing of Metals and Materials - Sohn International Symposium, San Diego USA (2006), arXiv, 2008. https://doi.org/10.48550/ARXIV.0803.2831.

[7] M.E. Choi, H.Y. Sohn, Development of green suspension ironmaking technology based on hydrogen reduction of iron oxide concentrate: rate measurements, Ironmak. Steelmak. 37 (2010) 81–88, https://doi.org/10.1179/030192309X12506804200663.

[8] A. Heidari, N. Niknahad, M. Iljana, T. Fabritius, A review on the kinetics of iron ore reduction by hydrogen, Materials 14 (2021) 7540, https://doi.org/10.3390/ma14247540.

[9] O. Kovtun, M. Levchenko, M.O. Ilatovskaia, C.G. Aneziris, O. Volkova, Results of hydrogen reduction of iron ore pellets at different temperatures, Steel Res. Int. (2024) 2300707, https://doi.org/10.1002/srin.202300707.

[10] D. Spreitzer, J. Schenk, Reduction of iron oxides with hydrogen—A review, Steel Research Int. 90 (2019) 1900108, https://doi.org/10.1002/srin.201900108.

[11] M. Bai, H. Long, L. Li, D. Liu, S.-B. Ren, C.-F. Zhao, J. Cheng, Kinetics of iron ore pellets reduced by H_2-N_2 under non-isothermal condition, Int. J. Hydrogen Energy 43 (2018) 15586–15592, https://doi.org/10.1016/j.ijhydene.2018.06.116.

[12] S. Hosokai, Y. Kasiwaya, K. Matsui, N. Okinaka, T. Akiyama, Ironmaking with ammonia at low temperature, Environ. Sci. Technol. 45 (2011) 821–826, https://doi.org/10.1021/es102910q.

[13] V. Vogl, M. Åhman, L.J. Nilsson, Assessment of hydrogen direct reduction for fossil-free steelmaking, J. Clean. Prod. 203 (2018) 736–745, https://doi.org/10.1016/j.jclepro.2018.08.279.

[14] S. Abanades, Redox cycles, active materials, and reactors applied to water and carbon dioxide splitting for solar thermochemical fuel production: a review, Energies 15 (2022) 7061, https://doi.org/10.3390/en15197061.

[15] S. Abanades, S. Rodat, H. Boujjat, Solar thermochemical green fuels production: a review of biomass pyro-gasification, solar reactor concepts and modelling methods, Energies 14 (2021) 1494, https://doi.org/10.3390/en14051494.

[16] S. Chuayboon, S. Abanades, An overview of solar decarbonization processes, reacting oxide materials, and thermochemical reactors for hydrogen and syngas production, Int. J. Hydrogen Energy 45 (2020) 25783–25810, https://doi.org/10.1016/j.ijhydene.2020.04.098.

[17] S. Abanades, H.I. Villafan-Vidales, CO_2 and H_2O conversion to solar fuels via two-step solar thermochemical looping using iron oxide redox pair, Chem. Eng. J. 175 (2011) 368–375, https://doi.org/10.1016/j.cej.2011.09.124.

[18] S. Abanades, H.I. Villafan-Vidales, CO_2 valorisation based on Fe_3O_4/FeO thermochemical redox reactions using concentrated solar energy, Int. J. Energy Res. 37 (2013) 598–608, https://doi.org/10.1002/er.1953.

[19] A. Steinfeld, P. Kuhn, J. Karni, High-temperature solar thermochemistry: Production of iron and synthesis gas by Fe_3O_4-reduction with methane, Energy 18 (1993) 239–249, https://doi.org/10.1016/0360-5442(93)90108-P.

[20] Q. Bellouard, S. Rodat, M. Grateau, S. Abanades, Solar biomass gasification combined with iron oxide reduction for syngas production and green iron metallurgy, Front. Energy Res. 8 (2020) 66, https://doi.org/10.3389/fenrg.2020.00066.

[21] S. Chuayboon, S. Abanades, S. Rodat, Stepwise solar methane reforming and water-splitting via lattice oxygen transfer in iron and cerium oxides, Energy Technol. 8 (2020) 1900415, https://doi.org/10.1002/ente.201900415.

[22] D. Fernández-González, J. Prazuch, Í. Ruiz-Bustinza, C. González-Gasca, J. Piñuela-Noval, L.F. Verdeja González, Iron metallurgy via concentrated solar energy, Metals 8 (2018) 873, https://doi.org/10.3390/met8110873.

[23] G. Levêque, S. Abanades, Thermodynamic and kinetic study of the carbothermal reduction of SnO_2 for solar thermochemical fuel generation, Energy Fuels 28 (2014) 1396–1405, https://doi.org/10.1021/ef402182g.

[24] H.I. Villafán-Vidales, S. Abanades, M. Montiel-González, H. Romero-Paredes-Rubio, Carbo- and methanothermal reduction of tungsten trioxide into metallic tungsten for thermochemical production of solar fuels, Energy Technol. 5 (2017) 692–702, https://doi.org/10.1002/ente.201600455.

[25] S. Chuayboon, S. Abanades, Clean magnesium production using concentrated solar heat in a high-temperature cavity-type thermochemical reactor, J. Clean. Prod. 232 (2019) 784–795, https://doi.org/10.1016/j.jclepro.2019.05.371.

[26] S. Chuayboon, S. Abanades, Solar metallurgy for sustainable Zn and Mg production in a vacuum reactor using concentrated sunlight, Sustainability 12 (2020) 6709, https://doi.org/10.3390/su12176709.

[27] S. Chuayboon, S. Abanades, Solar metallurgical process for high-purity Zn and syngas production using carbon or biomass feedstock in a flexible thermochemical reactor, Chem. Eng. Sci. 271 (2023) 118579, https://doi.org/10.1016/j.ces.2023.118579.

[28] S. Li, H. Zhang, J. Nie, R. Dewil, J. Baeyens, Y. Deng, The direct reduction of iron ore with hydrogen, Sustainability 13 (2021) 8866, https://doi.org/10.3390/su13168866.

[29] S. Chuayboon, S. Abanades, Green iron and syngas production via continuous solar-driven agricultural waste biomass gasification combined with iron(III) oxide reduction, Energy 306 (2024) 132432, https://doi.org/10.1016/j.energy.2024.132432.

[30] S. Abanades, S. Rodat, Solar-aided direct reduction of iron ore with hydrogen targeting carbon-free steel metallurgy, Renew. Energy 235 (2024) 121297, https://doi.org/10.1016/j.renene.2024.121297.

[31] T. Kodama, S. Bellan, N. Gokon, H.S. Cho, Particle reactors for solar thermochemical processes, Sol. Energy 156 (2017) 113–132, https://doi.org/10.1016/j.solener.2017.05.084.

[32] S. Bellan, T. Kodama, N. Gokon, K. Matsubara, A review on high-temperature thermochemical heat storage: particle reactors and materials based on solid–gas reactions, WIREs Energy Environ. 11 (2022), https://doi.org/10.1002/wene.440.

[33] L. André, S. Abanades, Recent advances in thermochemical energy storage via solid–gas reversible reactions at high temperature, Energies 13 (2020) 5859, https://doi.org/10.3390/en13225859.

[34] S. Abanades, A review of oxygen carrier materials and related thermochemical redox processes for concentrating solar thermal applications, Materials 16 (2023) 3582, https://doi.org/10.3390/ma16093582.

[35] M. Neises, S. Tescari, L. de Oliveira, M. Roeb, C. Sattler, B. Wong, Solar-heated rotary kiln for thermochemical energy storage, Sol. Energy 86 (2012) 3040–3048, https://doi.org/10.1016/j.solener.2012.07.012.

[36] E. Alonso, M. Romero, Review of experimental investigation on directly irradiated particles solar reactors, Renew. Sustain. Energy Rev. 41 (2015) 53–67, https://doi.org/10.1016/j.rser.2014.08.027.

[37] N. Gokon, S. Takahashi, H. Yamamoto, T. Kodama, Thermochemical two-step water-splitting reactor with internally circulating fluidized bed for thermal reduction of ferrite particles, Int. J. Hydrogen Energy 33 (2008) 2189–2199, https://doi.org/10.1016/j.ijhydene.2008.02.044.

[38] V. Nikulshina, C. Gebald, A. Steinfeld, CO_2 capture from atmospheric air via consecutive CaO-carbonation and $CaCO_3$-calcination cycles in a fluidized-bed solar reactor, Chem. Eng. J. 146 (2009) 244–248, https://doi.org/10.1016/j.cej.2008.06.005.

[39] S. Abanades, L. André, Design and demonstration of a high temperature solar-heated rotary tube reactor for continuous particles calcination, Appl. Energy 212 (2018) 1310–1320, https://doi.org/10.1016/j.apenergy.2018.01.019.
[40] E. Alonso, A. Gallo, M.I. Roldán, C.A. Pérez-Rábago, E. Fuentealba, Use of rotary kilns for solar thermal applications: review of developed studies and analysis of their potential, Sol. Energy 144 (2017) 90–104, https://doi.org/10.1016/j.solener.2017.01.004.
[41] M. Chambon, S. Abanades, G. Flamant, Design of a lab-scale rotary cavity-type solar reactor for continuous thermal dissociation of volatile oxides under reduced pressure, J. Sol. Energy Eng. 132 (2010) 021006, https://doi.org/10.1115/1.4001147.
[42] A. Steinfeld, A. Imhof, D. Mischler, Experimental investigation of an atmospheric-open cyclone solar reactor for solid-gas thermochemical reactions, J. Sol. Energy Eng. 114 (1992) 171–174, https://doi.org/10.1115/1.2930001.
[43] A. Steinfeld, M. Brack, A. Meier, A. Weidenkaff, D. Wuillemin, A solar chemical reactor for co-production of zinc and synthesis gas, Energy 23 (1998) 803–814, https://doi.org/10.1016/S0360-5442(98)00026-7.
[44] S. Abanades, H. Kimura, H. Otsuka, A drop-tube particle-entrained flow solar reactor applied to thermal methane splitting for hydrogen production, Fuel 153 (2015) 56–66, https://doi.org/10.1016/j.fuel.2015.02.103.
[45] A. Meier, E. Bonaldi, G.M. Cella, W. Lipinski, D. Wuillemin, R. Palumbo, Design and experimental investigation of a horizontal rotary reactor for the solar thermal production of lime, Energy 29 (2004) 811–821, https://doi.org/10.1016/S0360-5442(03)00187-7.
[46] R. Müller, P. Haeberling, R.D. Palumbo, Further advances toward the development of a direct heating solar thermal chemical reactor for the thermal dissociation of ZnO(s), Sol. Energy 80 (2006) 500–511, https://doi.org/10.1016/j.solener.2005.04.015.
[47] ANSYS, ANSYS FLUENT Theory Guide, Release 2021 R2, ANSYS, Canonsburg, PA, 2021.
[48] K.C. Mills, Y. Su, Z. Li, R.F. Brooks, Equations for the calculation of the thermo-physical properties of stainless steel, ISIJ Int. 44 (2004) 1661–1668, https://doi.org/10.2355/isijinternational.44.1661.
[49] F. Patisson, O. Mirgaux, J.-P. Birat, Hydrogen steelmaking. Part 1: physical chemistry and process metallurgy, Matér. Techn. 109 (2021) 303, https://doi.org/10.1051/mattech/2021025.